**An Acad Bras Cienc (2023) 95(Suppl. 3): e20210560 DOI 10.1590/0001-3765202320210560**
Anais da Academia Brasileira de Ciências | *Annals of the Brazilian Academy of Sciences*
Printed ISSN 0001-3765 I Online ISSN 1678-2690
www.scielo.br/aabc | www.fb.com/aabcjournal

**GEOSCIENCES**

# Sensitivity analysis of a King George Island outlet glacier, South Shetlands, Antarctica

THIAGO DIAS DOS SANTOS, MATHIEU MORLIGHEM, JEFFERSON CARDIA SIMÕES & PHILIPPE REMY BERNARD DEVLOO

**Abstract:** The Lange glacier is an outlet glacier situated in the Admiralty Bay, King George Island, Peninsula Antarctica. It retreated about 1 km since the 1950s. Although recent observations do not show any significant change at the ice-ocean margin, it is not clear whether this glacier has reached a new steady state or whether it is still adjusting to new climate conditions. By combining a three-dimensional glacier model with satellite and in-situ datasets, we investigate the sensitivity of Lange glacier to perturbations in flow rate factor, friction coefficient, surface mass balance, and calving front position. The (time-dependent) perturbation experiments show that the glacier is more sensitive to changes in surface mass balance and in flow rate factor. These results suggest that the climate variability of this region plays an important role on the glacier's dynamics, and that measurements of englacial temperature will improve the reliability of future modeling efforts. Our model shows that the position of the ice front exerts a strong control on the glacier flux. In our time-dependent simulation, the impacts of the observed front retreat on the glacier's dynamics persist beyond the present date. This suggests that Lange is likely still adjusting to past perturbations at its terminus.

**Key words:** King George Island, Lange glacier, numerical simulation, sensitivity analysis.

## INTRODUCTION

King George Island (KGI, Fig. 1), in the Antarctic Peninsula, has experienced an increase in air temperature over the last six decades (Ferron et al. 2004, Turner et al. 2005, 2016, Bers et al. 2013, Kejna et al. 2013, Gonzalez & Fortuny 2018, Thomas & Tetzner 2019). Although short periods of cooling have been observed since the 1990s (Carrasco 2013, Turner et al. 2016, Oliva et al. 2017), likely due to natural variability (Turner et al. 2016, Gonzalez & Fortuny 2018), the air temperature has been increasing by 0.3-0.5 °C per decade since the 1950s (Comin & Justino 2017, Gonzalez & Fortuny 2018, Thomas & Tetzner 2019). During the same period, most glaciers situated on KGI experienced retreat, thinning, and an increase in surface melt (Simões et al. 1999, 2004a, 2015, Cook et al. 2005, Rückamp et al. 2011, Barrand et al. 2013, Falk et al. 2018b, Pudełko et al. 2018, Sziło & Bialik 2018, Rosa et al. 2020, Pasik et al. 2021), which have been associated to regional warming (Kejna et al. 1998, Park et al. 1998, Simões et al. 2004a, Falk et al. 2018b, Rosa et al. 2020, Silva et al. 2020, Pasik et al. 2021). Lange glacier is a fast tidewater glacier situated in the Admiralty Bay along the southern coast of KGI (Fig. 1). This glacier has been changing dramatically over the past decades: it has retreated by at least 1 km since 1950 (Macheret & Moskalevsky 1999, Simões et al. 1999) (see Fig. 2) and its surface velocities are

today reaching up to 1.5 m per day (e.g., Schwalbe et al. 2020). Although today's field observations do not indicate any change in frontal position or surface velocity (e.g., Johnson et al. 2020), it is not clear whether this glacier reached a new steady state or whether it is still adjusting to new climate conditions.

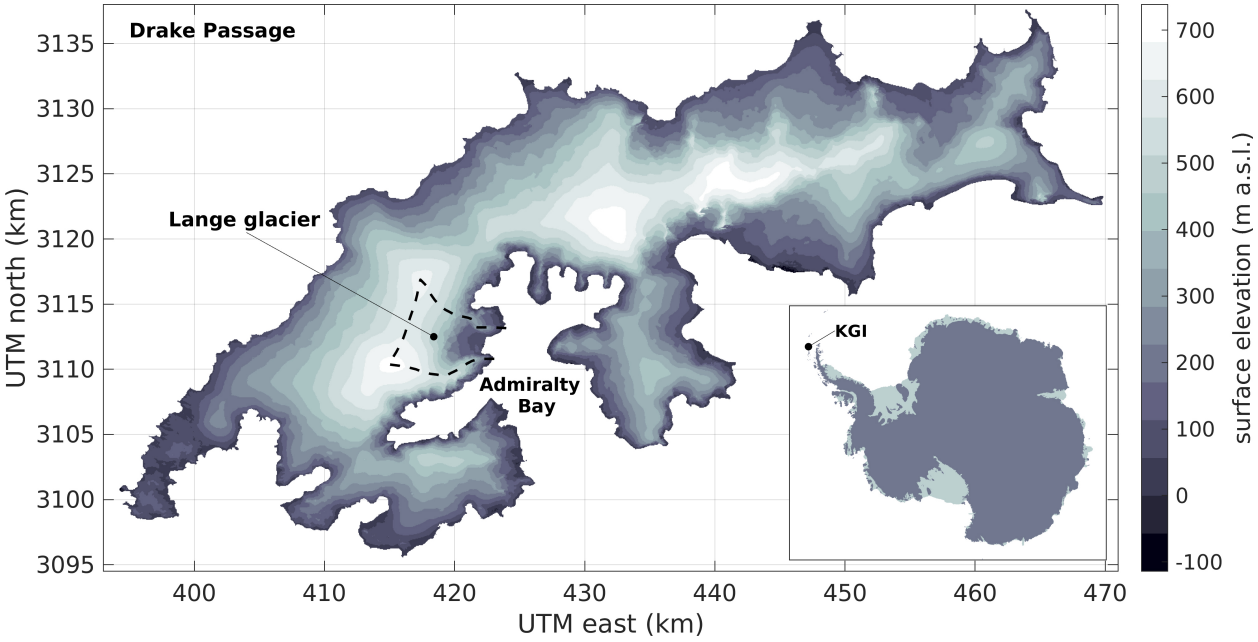


**Figure 1. Location and surface elevation (meters above sea level) of King George Island (KGI), Antarctic Peninsula. Dashed-black lines delineate the Lange glacier (basin). The KGI surface elevation is derived from TanDEM-X satellite data (Braun et al. 2016).**

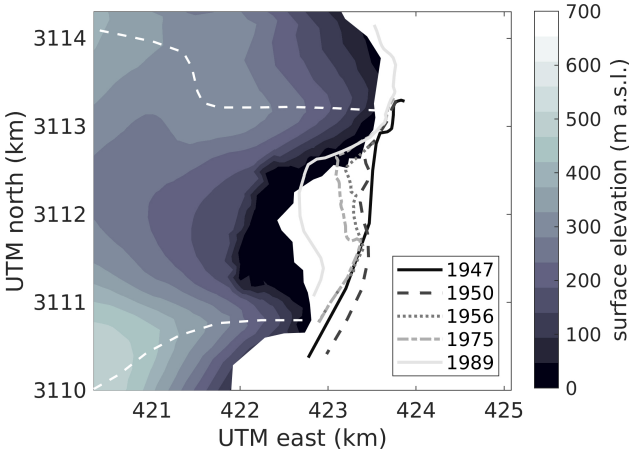


**Figure 2. Historical retreat of calving front, Lange glacier. The calving front positions are extracted from the Antarctic Digital Database project of the Scientific Committee on Antarctic Research (SCAR-ADD 2021). The surface elevation shown here is derived from TanDEM-X satellite data (Braun et al. 2016).**

Several studies investigated the dynamics and sensitivities of the glaciers on KGI and neighboring islands to climate forcings (Knap et al. 1996, Barboza et al. 2004, Martín et al. 2004, Breuer et al. 2006, Lee et al. 2008, Otero et al. 2010, Rückamp et al. 2010, Davies et al. 2014). All of them relied on numerical models that computed the ice velocities and the glacier evolution through time. To improve the reliability and accuracy of the numerical model, some of these studies performed a

'static model calibration', where an ice flow parameter like ice rheology or basal friction are tuned such that the computed ice velocities matches observed surface velocities within an acceptable tolerance (Martín et al. 2004, Breuer et al. 2006, Rückamp et al. 2010). Others, due to the lack of spatial data, employed a 'time-dependent calibration' (or 'dynamic model calibration'), where the final glacier geometry is compared to the current digital elevation model (DEM) and/or geomorphological features of past glacial landforms (e.g., moraines, Davies et al. 2014). In the former, only the ice velocity computation is required, whereas for the latter, the parameter tuning involves computations of both velocity and thickness evolution which may better constrain the current glacier state (e.g., Pollard & DeConto 2012, Davies et al. 2014). By employing static calibration, previous numerical modeling of Lange and neighboring glaciers considered a polythermal ice structure over the ice body (Simões et al. 2004b, Blindow et al. 2010, Travassos et al. 2012) to match observed ice surface velocities (Barboza et al. 2004, Breuer et al. 2006, Rückamp et al. 2010). However, it remains unclear whether temperate conditions at the ice-bedrock interface, where basal sliding may occur, play an important role in Lange's dynamics. Also, the respective importance of ice flow parameters and changes in climate forcings on the dynamics of Lange is not well understood. Quantifying the sensitivity to these factors helps guide future efforts in projecting the dynamics and discharge of the KGI ice cap.

Here we construct a numerical model to investigate the dynamics and the sensitivity of Lange glacier to changes in internal properties (rheological and basal friction parameters) as well as external forcings (surface mass balance and ice front position). We also investigate the glacier's response under some hypothetical climate scenarios after constraining the initial conditions by imposing observed changes in calving front position. Besides, we quantify the impact of observed front retreat on the glacier discharge. Ice thickness, bed topography, and satellite-derived and in-situ measurements of surface velocity are obtained from Rückamp et al. (2010), Rückamp & Blindow (2012), Osmanoğlu et al. (2013), Falk et al. (2016), Schwalbe et al. (2020). Annual ice accumulation rates are derived from several available datasets (e.g., Rückamp et al. 2011, Falk et al. 2018a). We use the Ice-sheet and Sea-level System Model (ISSM, Larour et al. 2012) to model the evolution of the glacier geometry and ice velocity. We employ a dynamic model calibration to tune the basal friction in order to match today's surface elevation, and compare with a hypothetical case where the ice-bedrock interface is frozen (i.e., basal velocity equal to zero), as assumed in previous studies (e.g., Barboza et al. 2004).

## MATERIALS AND METHODS

### Glaciological data

The bed topography and surface digital elevation model (DEM) of KGI is derived from ground penetrating radar (GPR) and from differential GPS (DGPS) measurements carried out by different field campaigns. These measurements were combined by Rückamp & Blindow (2012). The reference year employed for the Lange's DEM is 2010. The dataset comprises elevations of the bedrock and ice surface at a horizontal resolution of 50 m. The bathymetry of the Admiralty Bay is derived from seismic samples performed by the Brazilian Antarctic Program (PROANTAR, Magrani & Neto 2014), which connects to the bedrock elevation at Lange's ice front. We use the 2010 DEM to calibrate the numerical model (see the model calibration section). The basin of Lange is delineated according to the surface elevation

**Table I. Parameters used in the numerical experiments.**

| Parameter | Value | Description |
|---|---|---|
| $a$ | 4.90 mm w.e./yr | reference surface mass balance slope |
| $b$ | -911.37 mm w.e./yr | reference surface mass balance at sea level |
| ELA | 186 m a.s.l. | reference equilibrium line altitude |
| $A$ | $2.3 \times 10^{-24}$ Pa$^{-3}$ s$^{-1}$ | reference flow rate factor |
| $\rho$ | 918 kg/m$^3$ | ice density |
| $\rho_w$ | 1028 kg/m$^3$ | ocean water density |
| $\rho_{fw}$ | 1000 kg/m$^3$ | fresh water density |
| $g$ | 9.81 m/s$^2$ | gravity acceleration |
| $n$ | 3 | Glen's law exponent |
| $S_0$ | 600 m | dynamic inversion scaling parameter |

and surface gradient. The glacier area is ∼28 km$^2$ (Osmanoğlu et al. 2013), with total ice volume equal to 7.1 km$^3$.

Observed surface velocities are derived from DGPS (Rückamp et al. 2010), from synthetic aperture radar (SAR, Falk et al. 2016, Osmanoğlu et al. 2013), and from stereo-photogrammetric measurements (Schwalbe et al. 2020), and are used for model validation.

The historical retreat of Lange's calving front is a compilation of different coastline measurements of KGI that have been taken since 1947. The sources of these measurements are shown in Table 7B of Ferrigno et al. (2006), and the Antarctic Digital Database project of the Scientific Committee on Antarctic Research (SCAR-ADD 2021) has made this dataset available in digital format. We extracted the calving front positions of Lange from the SCAR-ADD (2021) (see Fig. 2).

The surface mass balance (SMB), $\dot{m}_s$, is derived from several field measurements of ice accumulation/ablation at KGI (Zamoruyev 1972, Orheim & Govorukha 1982, Bintanja 1995, Wen et al. 1998, Han et al. 1999, Braun et al. 2001, 2004, Simões et al. 2004b, Rückamp et al. 2011). These measurements consist of in-situ estimates of mass balance at some specific locations of KGI. For modeling purposes, instead of interpolating these measurements over the entire glacier domain, we assume the SMB to be linearly changing with height, $z$, as follows:

$$\dot{m}_s = a\, z + b, \tag{1}$$

where $a$ and $b$ are constants. Here, we adjust $a$ and $b$ by linear regression considering the field measurements of SMB. The adjusted values of $a$ and $b$ are shown in Table I, and are referred to as the 'reference surface mass balance parameters'. From Eq. 1, we obtain an adjusted equilibrium line altitude (ELA) equal to ∼186 m, referred to as the 'reference ELA', which is within the range of values reported for KGI glaciers (140-290 m a.s.l., e.g., Orheim & Govorukha 1982, Jiawen et al. 1995, Sobota et al. 2015, Pudełko et al. 2018, Pasik et al. 2021). Figure 3 shows the observed surface mass balance and the adjusted reference surface mass balance as well as the adjusted reference ELA.

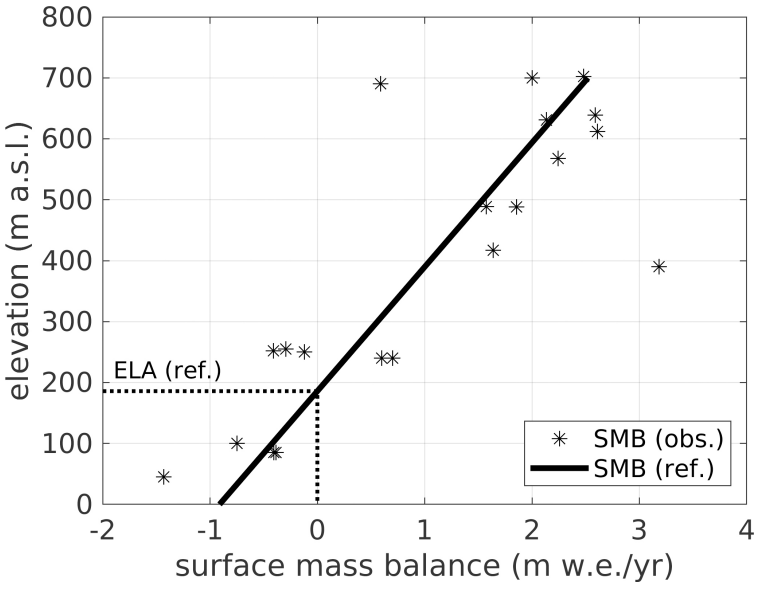


**Figure 3. Surface mass balance (SMB) of KGI. Asterisks are observed surface mass balance. The solid line is the adjusted surface mass balance using Eq. 1 ('reference SMB') employed in the numerical model of Lange glacier. The dotted line shows the equilibrium line altitude (ELA) obtained with the reference SMB, ('reference ELA'). See Table I for details.**

## Ice flow model

The dynamics of Lange glacier is modeled by two set of equations: the stress balance equation and the mass transport equation. The first equation provides the velocity field over the entire glacier for a given geometry (surface, base, ice-ocean boundary), and the second one updates the ice geometry over time based on mass conservation. Here, we employ the Blatter-Pattyn (BP) model for the stress balance equation, defined as (Blatter 1995, Pattyn 2003):

$$\begin{aligned}\frac{\partial}{\partial x}\left(4\mu\frac{\partial u_x}{\partial x}+2\mu\frac{\partial u_y}{\partial y}\right)+\frac{\partial}{\partial y}\left(\mu\frac{\partial u_x}{\partial y}+\mu\frac{\partial u_y}{\partial x}\right)+\frac{\partial}{\partial z}\left(\mu\frac{\partial u_x}{\partial z}\right)=\rho g\frac{\partial s}{\partial x},\\ \frac{\partial}{\partial x}\left(\mu\frac{\partial u_x}{\partial y}+\mu\frac{\partial u_y}{\partial x}\right)+\frac{\partial}{\partial y}\left(4\mu\frac{\partial u_y}{\partial y}+2\mu\frac{\partial u_x}{\partial x}\right)+\frac{\partial}{\partial z}\left(\mu\frac{\partial u_y}{\partial z}\right)=\rho g\frac{\partial s}{\partial y},\end{aligned} \tag{2}$$

where $u_x$ and $u_y$ are the horizontal ice velocities, $\mu$ is the non-linear ice viscosity, $\rho$ is the ice density, $s$ is the ice surface elevation, and $g$ is the gravity acceleration. The values of $\rho$ and $g$ are shown in Table I. The ice viscosity is given by the Glen's law:

$$\mu=\frac{B}{2\dot{\varepsilon}_e^{1-1/n}}=\frac{1}{2A^{1/n}\dot{\varepsilon}_e^{1-1/n}}, \tag{3}$$

with $B=A^{-1/n}$ (or $A=B^{-n}$), where $A$ is the rate factor, $B$ is the associated rate factor or ice rigidity, $n=3$, and $\dot{\varepsilon}_e$ is the effective strain tensor, defined as:

$$\begin{aligned}\dot{\varepsilon}_e=\Bigg[&\left(\frac{\partial u_x}{\partial x}\right)^2+\left(\frac{\partial u_y}{\partial y}\right)^2+\frac{\partial u_x}{\partial x}\frac{\partial u_y}{\partial y}+\frac{1}{2}\frac{\partial u_x}{\partial y}\frac{\partial u_y}{\partial x}\\ &+\frac{1}{4}\left(\frac{\partial u_x}{\partial y}\right)^2+\frac{1}{4}\left(\frac{\partial u_y}{\partial x}\right)^2+\frac{1}{4}\left(\frac{\partial u_x}{\partial z}\right)^2+\frac{1}{4}\left(\frac{\partial u_y}{\partial z}\right)^2\Bigg]^{1/2}.\end{aligned} \tag{4}$$

The right-side terms of Eq. 2 are named as the 'driving forcings', i.e., the forces that drive the glacier to flow downwards. We note that the BP model, Eq. 2, describes the horizontal force balance where

only the horizontal velocities are computed. The vertical velocity, $u_z$, is retrieved by the continuity equation:

$$\frac{\partial u_x}{\partial x} + \frac{\partial u_y}{\partial y} + \frac{\partial u_z}{\partial z} = 0. \tag{5}$$

The boundary conditions are specified at the ice base and at the ice front. For the base, a basal drag ($\tau_b$) due to basal slip is modeled using a Budd-type friction law (Budd et al. 1979):

$$\tau_b = -C^2 N \mathbf{u}_b, \tag{6}$$

where $C$ is the friction coefficient, $N$ is the effective pressure at the ice-bed interface, and $\mathbf{u}_b$ are the horizontal velocities at the base. Here, the friction coefficient is adjusted spatially using a dynamic inversion (see the model calibration section). At the ice front, we apply ocean water pressure.

Solving Eq. 2 and Eq. 5 yields the ice velocities over the entire glacier. The mass transport equation is given by a vertically integrated transport equation defined as:

$$\frac{\partial H}{\partial t} = -\frac{\partial}{\partial x}\left(u_x H\right) - \frac{\partial}{\partial y}\left(u_y H\right) + \dot{m}_s - \dot{m}_b\,, \tag{7}$$

where $H\,(= s - b)$ is the ice thickness ($b$ is the base elevation), $u_x H$ and $u_y H$ are the components of the horizontal mass flux, $\dot{m}_s$ is the surface mass balance (positive for accumulation), and $\dot{m}_b$ is the basal melting (positive if ablation). As described in the glaciological data section, we assume that the surface mass balance varies with the vertical coordinate $z$, which means that variations in ice surface will change the rate of accumulation/ablation of the glacier. This non-linear feedback is accounted in our model through Eq. 1 (by setting $z = s$). Basal melt is generally negligible under grounded ice and, therefore, we set here $\dot{m}_b = 0$. Note that, despite neglecting basal melting, we still consider basal sliding at the ice-bedrock interface (see the model calibration section for details).

We employ the Ice-sheet and Sea-level System Model (ISSM, Larour et al. 2012) to solve both the BP and thickness equations within a finite element method framework. During our transient simulations, Lange's basin can migrate, and the interactions with neighboring glaciers could change the velocities and geometry along Lange's boundaries. In order to circumvent any numerical error due to the definition of boundary conditions, and to take into account the glaciers' interactions, we extend the horizontal model domain across the glaciers that could affect Lange's dynamics (e.g., see Fig. 5). The horizontal domain is discretized using triangle-based elements with different spatial resolutions. A resolution equal to 150 m is applied at Lange's front, including the fastest area of the glacier as well as the region of the Admiralty Bay where the calving front was located in the past (Fig. 2), and a 350-m resolution is employed on the rest of the glacier's basin. Elsewhere, in order to reduce the computational cost, we vary the mesh resolution from 350 m to 2 km. To build the three-dimensional model, we extrude the horizontal mesh vertically from the ice base to the ice surface. The vertical coordinate is divided by nine equally-spaced layers (defined after a mesh resolution analysis, not shown here), creating eight prismatic elements along the ice thickness. The final mesh contains about 44,000 prismatic elements and 26,000 vertices. We employ P1-Lagrange elements to solve both sets of equations (Eq. 2 and Eq. 7).

## Model calibration

For the model calibration, we perform a dynamic inversion based on the work of Pollard & DeConto (2012). The method consists of adjusting spatially a parameter (e.g., friction coefficient) during a transient simulation, and the misfit between the observed and modeled surface elevations is used as a correction to apply to the parameter (e.g., increase basal friction where the model is too thin and decrease basal friction where the model is too thick). After the inversion (calibration), the modeled ice velocity is compared to the observed velocity as a secondary verification (i.e., a model validation). Here, we run the model for 1,000 years, and adjust the parameter every 25 years.

We consider two different cases for the model calibration. The first one considers a slippery bed condition, where basal sliding may occur. This is an expected condition for Lange glacier (e.g., Pęcherzewski 1980, Pichlmaier et al. 2004, Blindow et al. 2010, Rückamp et al. 2010, Aquino FE, unpublished data). This is the case employed in the numerical experiments (sensitivity and centennial response analyses). The second case consists of a no basal sliding condition for which the velocities at the glacier base are set to zero (i.e., $\mathbf{u}_b = \mathbf{0}$). This case is based on previous studies (e.g., Barboza et al. 2004) and performed here for comparison purposes (i.e., only to compare with the slip bed case).

For the case where the ice is allowed to slide over the bedrock, we adjust the friction coefficient $C$. Here, we initialize the coefficient as $C = 100\ \mathrm{s}^{1/2}\,\mathrm{m}^{-1/2}$ everywhere, and we correct it, for each vertex at the glacier base, as follows:

$$\begin{aligned} C^{i+1} &= C^i \sqrt{10^{\Delta z}}, \\ \Delta z &= \max\left(-1.5,\ \min\left(1.5,\ \Delta S / S_0\right)\right), \\ \Delta S &= S_{obs} - S_{mod}, \\ i &= 1,\ 2,\ \ldots,\ n_s, \end{aligned} \tag{8}$$

where $S_0$ is a scaling parameter, and $S_{obs}$ and $S_{mod}$ are the observed and modeled ice surface elevations, respectively, defined at each vertex of the ice surface. We use $S_0 = 600$ m. The total number of adjustments, $n_s$, is equal to 40 (=1000 years/25 years). At each step $i$, we compare the relative mean surface misfit with a tolerance, and we stop the process if this threshold is achieved. We use the reference flow rate factor (Table I) over the entire ice cap, and the surface mass balance is defined according to the reference ELA (also in Table I).

For the case with no basal sliding, we tune the flow rate factor (ice rigidity $B$) by using the same approach (Eq. 8), as follows:

$$\begin{aligned} B^{i+1} &= \max\left(B_{min},\ B^i 10^{\Delta z}\right), \\ \Delta z &= \max\left(-1.1,\ \min\left(1.1,\ \Delta S / S_0\right)\right), \\ \Delta S &= S_{obs} - S_{mod}, \\ i &= 1,\ 2,\ \ldots,\ n_s. \end{aligned} \tag{9}$$

We enforce a minimum value of $B$ of $B_{min} = 4.74 \times 10^7\ \mathrm{Pa\,s}^{1/3} = 0.15\ \mathrm{MPa\,yr}^{1/3}$ (or, equivalently, $A_{max} = 9.40 \times 10^{-24}\ \mathrm{Pa}^{-3}\,\mathrm{s}^{-1}$), which is slightly smaller than the minimum $B$ reported for neighboring islands (e.g., Martín et al. 2004). Here, $A_{max}$ represents a flow rate factor with water content of about 1% according to the Duval's relation (Duval 1977, Cuffey & Paterson 2010, p. 66):

$$A_w = (3.2 + 5.8w) \times 10^{-15}\ \mathrm{kPa}^{-3}\mathrm{s}^{-1}, \tag{10}$$

where $w$ is the water content in %. We do not consider vertical variations of the flow rate factor, in contrast to previous studies that considered heterogeneous distribution of water content and/or a cold-temperate transition surface (Martín et al. 2004, Breuer et al. 2006, Rückamp et al. 2010). Due to the lack of observations covering the entire glacier, and to avoid adding further complexity to the model, we adopt a scenario where $B$ ($A$) varies only horizontally in Eq. 9. We also rely on the reference surface mass balance in this model calibration.

## Sensitivity experiments

The sensitivity experiments are transient simulations forced by changes (perturbations) in some model parameters. We start the models from the same initial conditions (the state achieved by the model calibration considering slippery bed condition), apply a perturbation and run forward in time for several years, and we compare the final ice volume. To define the amount of time ($t$) to run, we use an estimated volume time scale defined as (Jóhannesson et al. 1989):

$$\tau = -\frac{\bar{H}}{\dot{m}_s(x = L)}, \tag{11}$$

where $\bar{H}$ is a characteristic ice thickness (e.g., mean thickness), and $\dot{m}_s(x = L)$ is the mass balance at the glacier terminus. For Lange, we have $\bar{H} \sim 160$ m and $\dot{m}_s(x = L) \sim -1$ m/yr (using $b$ and densities of ice and fresh water shown in Table I), which leads to $\tau \sim 160$ years. We define $t = 500$ years $\sim 3\tau$, which is enough to reach a state close to steady state after a perturbation is applied.

We choose model parameters that are somehow impacted by changes in climate. For instance, with increasing atmospheric temperatures, we expect the ELA to rise, the flow rate factor to increase (due to increased water content and warmer ice temperature), the friction coefficient to decrease (due to enhanced basal lubrication), and the glacier to retreat. In order to determine the sensitivity of the glacier to a changing climate, we therefore apply variations in flow rate factor ($A$), friction coefficient ($C$), ice front position, and in the ELA. Table II shows the minimum and maximum values (range of changes) employed for each parameter. The reference values are also shown in Table II. We define the range of changes based on some physical assumptions, observations or some percentage around the reference value. For example, for the flow rate factor $A$, the minimum value corresponds to a creep parameter at ∼-4.5 °C (Cuffey & Paterson 2010, p. 75), whereas the maximum value is based on temperate ice (0 °C) and a water content of 0.6% (Eq. 10). The variation in the friction coefficient corresponds to ±30% around the reference value. In this case, we apply the same scaling factor over the entire domain and, for simplicity, we only present the average coefficient in Table II. For ice front variations, the maximum value corresponds to the observed position in the 1950s. The most retreated position is achieved by applying a retreat of about 1.2 km in comparison to the reference position, whose magnitude is similar to the retreat experienced since 1950. Changes in ELA present a relatively large range of perturbation, which is based on the climate variability observed on KGI (see Fig. 3).

The ice front is fixed in time during all transient simulations. For the ice front perturbation experiment, the front position is manually changed at the beginning of the experiment, and kept fixed after that. All experiments employ the reference values for all other model parameters.

**Table II. Range of changes for sensitivity experiments.**

| Parameter | Reference value | Range of changes |
|---|---|---|
| $A$ | $2.3 \times 10^{-24}$ Pa$^{-3}$ s$^{-1}$ | 1.0 to 6.7 $\times 10^{-24}$ Pa$^{-3}$ s$^{-1}$ |
| $C$ (mean) | 1300 s$^{1/2}$ m$^{-1/2}$ | 900 to 1700 s$^{1/2}$ m$^{-1/2}$ |
| Front pos. | 6 km | 4.8 to 7.5 km |
| ELA | 186 m a.s.l. | -18 to 390 m a.s.l. |

## Centennial response projections

The centennial response of Lange glacier to changes in climate forcings (future enhanced warming) consists of transient simulations starting in 2010 and ending in 2200 forced by different ELA scenarios. In these simulations, instead of starting from the end of the model calibration (as performed in the sensitivity analysis), we constrain the initial state (2010) by imposing changes in calving front position according to observations (Fig. 2). The rationale for this constraint is to improve the initial glacier mass trend, which is not necessarily captured by our model calibration, since the ice-ocean boundary is kept fixed during the calibration. Another reason is to analyze the impact of the observed front retreat over time beyond 2010.

A map of the Admiralty Bay from the Antarctic French expedition in 1908-1910 (Bongrain & Godfroy 1912) indicates that Lange's front was close to its 1950 position, suggesting that it had been stationary for several decades prior to 1950. To overcome the lack of observations, we assume that the glacier was close to steady state in the 1910-1950 period. Under this *ad hoc* assumption, we manually change the calving front to match the 1950 position, and, starting from the state obtained after model calibration with slippery bed condition, we forward in time until the glacier reaches steady state. We employ the reference ELA to achieve this stationary condition.

From 1950 to 2010, we force the model with the reference ELA and with the observed changes in calving front position (Fig. 2). The calving front changes are manually imposed in the model by changing the ice-ocean boundary. Calving dynamics is not considered in this work. Following the available calving-front time series, we divide the simulation time from 1950 to 2010 in specific periods, as shown in Table III. The changes in ice front position are applied at the beginning of each period.

Once the 2010 state is reached, we run forward in time until 2200 under different step-wise changes in ELA, simulating different warming scenarios. We run with ELA=186 (reference), 230, 330, and 430 m a.s.l. Although these abrupt changes in ELA may not be realistic, they allow us to estimate an upper glacier response to climate forcings scenarios. In order to quantify the effect of increased calving rate (regardless the effect of increasing the ablation zone by changes in SMB), we run additional experiments where we impose a front retreat of $\sim$650 m from the 2010 terminus.

**Table III. Centennial response analysis: time periods for which the calving front position is updated according to observations (from 1950 to 2010). Periods #0 to #5 constrain the initial condition for the centennial simulations (#6a and #6b).**

| # | Time period | Description |
|---|---|---|
| 0 | 1910-1950 | 1950 calving front and reference ELA (steady state) |
| 1 | 1950-1956 | 1950 calving front and reference ELA |
| 2 | 1956-1975 | 1956 calving front and reference ELA |
| 3 | 1975-1989 | 1975 calving front and reference ELA |
| 4 | 1989-2000 | 1989 calving front and reference ELA |
| 5 | 2000-2010 | 2000 calving front and reference ELA |
| 6a | 2010-2200 | 2010 calving front and several ELA scenarios |
| 6b | 2010-2200 | retreat of calving front and several ELA scenarios |

## RESULTS

In the dynamic model calibration, considering no basal sliding (i.e., basal velocity set to zero) and adjusting the ice flow factor to match the 2010 surface geometry, the model overestimates Lange's surface elevation by up to ∼100 m in regions close to the glacier's terminus (Fig. 4a). Over those regions, the adjusted flow rate reaches up to $A = 9.4 \times 10^{-24}$ Pa$^{-3}$ s$^{-1}$, i.e., the maximum value allowed in the calibration algorithm. The resulting volume is 7.7 km$^3$, ∼8% higher compared to the 2010 estimated volume (7.1 km$^3$). On the other hand, if we allow the glacier to slide over the bed and dynamically tune the friction coefficient, the model reproduces the 2010 ice surface within a relatively small average misfit of ∼12 m, and a resulting volume of 6.7 km$^3$, which is about 6% less than the 2010 estimated volume (Fig. 4a).

In terms of surface velocities, in the model calibration case with no basal slip, the model underestimates the ice velocities in comparison to in-situ measurements, mainly after kilometer 3, as shown along the flow line shown in Fig. 4b. Alternatively, the dynamic calibration considering a slippery bed generates surface velocities in agreement with in-situ measurements within an acceptable tolerance, as also shown in Fig. 4b. At the glacier terminus, the satellite-derived velocity is between 300 and 550 m/yr (Osmanoğlu et al. 2013, Falk et al. 2016) and stereo-photogrammetric measurements estimate a peak of ∼550 m/yr (Schwalbe et al. 2020), while the modeled surface velocity is ∼450 m/yr. The modeled ice discharge is 0.031 Gt/yr, which is within the same order of magnitude as a satellite-based estimates, 0.013-0.024 Gt/yr (Osmanoğlu et al. 2013, Johnson et al. 2020). These differences may be attributed to differences in the location of the flux gate and ice thickness in which the discharge is computed. In Fig. 4b, the basal velocity is negligible in the first two kilometers of the flow line. In this region, the flow is dominated by ice internal deformation (i.e., vertical shear). Between 2 and 4 km downstream, the ice flow is controlled by both basal sliding and internal deformation, as seen in the difference between the basal and surface velocities in Fig. 4b. This region coincides with the location of the main crevasses observed in Lange. Downstream of kilometer 4, the glacier starts

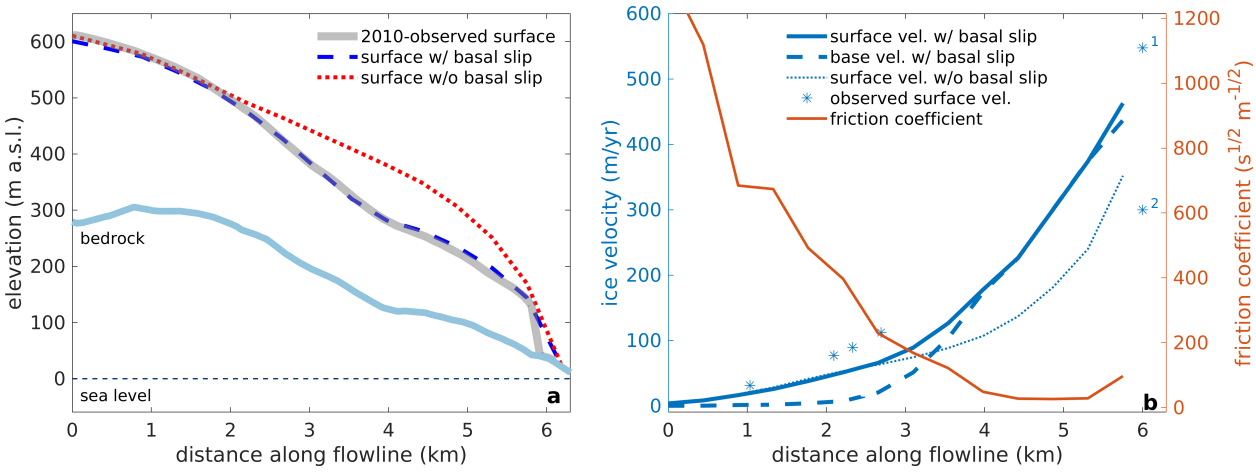


**Figure 4. Results of the dynamic model calibration along a flow line. Figure (a) shows a surface elevation comparison. The solid gray line is the 2010 observed ice surface (Rückamp & Blindow 2012). The red-dotted line is the surface obtained by dynamic calibration considering no basal sliding. The adjusted ice rheology for this case reaches up to $A = 9.4 \times 10^{-24}$ Pa$^{-3}$ s$^{-1}$ in regions close to the glacier's terminus. The dashed-blue line is the ice surface obtained by assuming basal slip and ice rheology equal to $A = 2.3 \times 10^{-24}$ Pa$^{-3}$ s$^{-1}$ over the entire ice cap. Figure (b) shows an ice velocity comparison. The blue-dotted line is the surface velocity after model calibration considering only ice internal deformation (i.e., no basal sliding). The blue-solid line is the surface velocity after model calibration taking into account basal sliding. The blue-dashed line is the base velocity obtained with this model calibration. The blue asterisks are in-situ measurements of surface velocities (Rückamp et al. 2010), except at the terminus (kilometer 6), where the velocities were obtained by both satellite-derived data and stereo-photogrametric measurement: (1) is from Falk et al. (2016) and Schwalbe et al. (2020), and (2) is from Osmanoğlu et al. (2013). The position along flow line of (2) is estimated. The orange line is the friction coefficient obtained by the model calibration.**

to slide more such that the ice flow is comparable to a 'plug-flow' regime, and the glacier's surface velocity is dominated mostly by basal sliding rather than internal deformation.

Also in Fig. 4b, the tuned friction coefficient decreases linearly between the ice divide and kilometer 4, reducing to a minimum value downstream of this point. The dynamic inversion reveals that relatively high values of friction coefficient ($> 600$ s$^{1/2}$ m$^{-1/2}$) are found along the basin divide, as seen in Fig. 5b. The basal velocities are close to zero on these regions, increasing up to 400 m/yr or higher as the ice flows to the Admiralty Bay (Fig. 5c), contributing to an increased surface velocity (Fig. 5d). In our model, about 50% of Lange's basin flows at a speed higher than 1 m/yr; the ratio of areas where basal velocities exceed 0.5 m/yr increases to 60%, and virtually 80% of the glacier basin has basal velocities higher than 0.1 m/yr.

In the sensitivity analysis, the volume of the glacier at the end of the experiments (i.e., after 500 years) depends on the parameter perturbed, varying roughly from 4 to 8 km$^3$ (Fig. 6). For changes in the flow rate factor (Fig. 6a), the ice volume decreases to 5.5 km$^3$ for $A = 6.7 \times 10^{-24}$ Pa$^{-3}$ s$^{-1}$. A non-linear relation appears between the total ice volume and the flow rate factor, $A$ (Fig. 6a). This is expected given the non-linear dependence of the ice viscosity on the flow rate parameter and ice strain rate (Eq. 3). Reducing $A$ to $10^{-24}$ Pa$^{-3}$ s$^{-1}$, i.e., making the ice stiffer, the ice volume increases to 7.8 km$^3$. Changes in friction coefficient lead to a smaller range of volume changes: the volume varies between 6.2 and 7.1 km$^3$ for a variation of 30% around the reference value (Fig. 6b). A similar range of volume

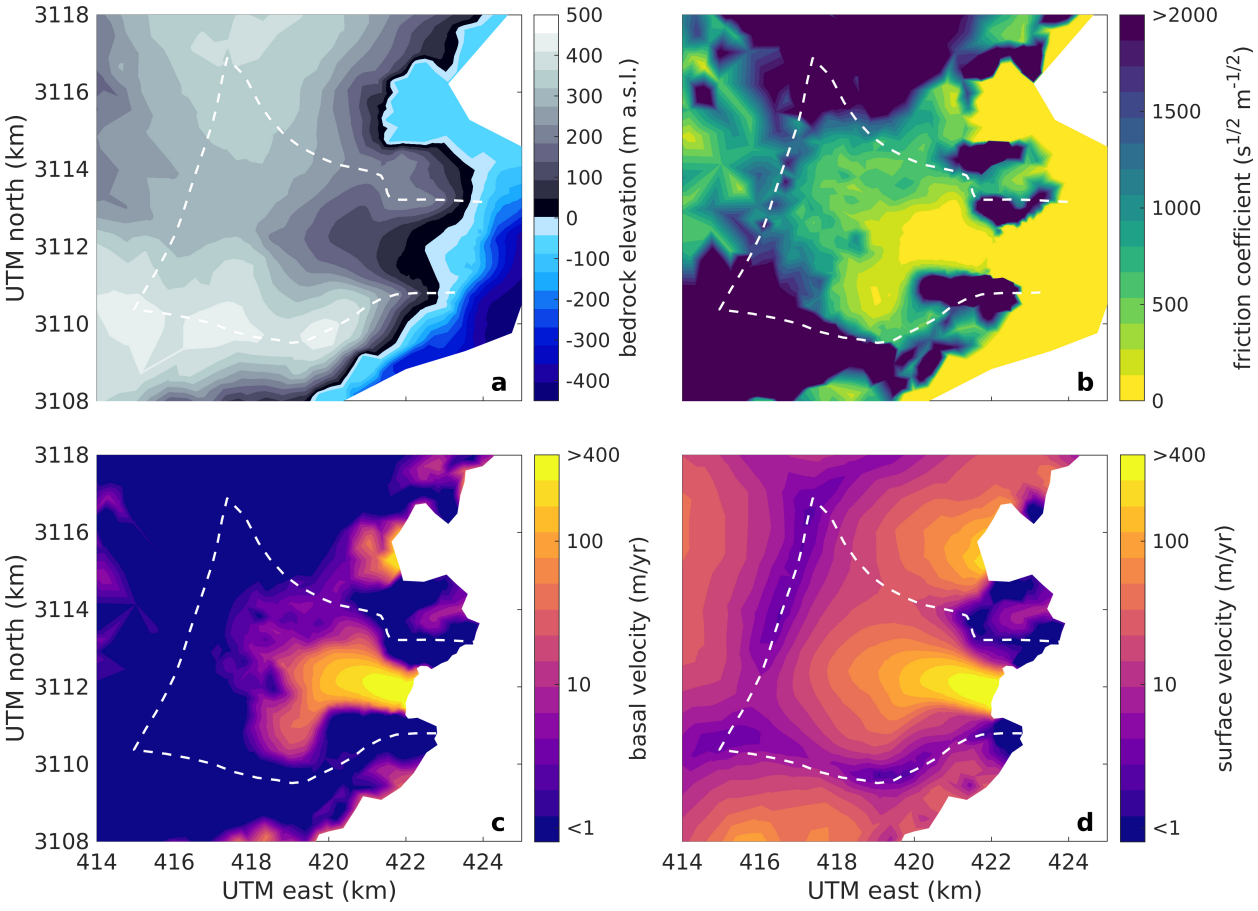


**Figure 5. Results of the dynamic model calibration: (a) bedrock elevation and Admiralty Bay bathymetry (Rückamp & Blindow 2012, Magrani & Neto 2014), (b) calibrated friction coefficient, (c) and (d) are the modeled basal and surface velocities, respectively, at the end of the model calibration. The dashed-white lines delineate Lange's basin.**

change is observed for ice front position perturbations (Fig. 6c), and the volume sensitivity to front retreat is nearly linear, i.e., the volume change is virtually proportional to the amount of imposed front change. Changes in the terminus position affects the amount of basal and lateral resistance transmitted upstream, impacting the entire glacier flow. Considering the 1950 front position, Lange gains 6% in volume in comparison to the reference front position, reaching 7.1 km$^3$. Imposing a front retreat of 1.2 km, and therefore reducing basal and lateral resistance, leads to an ice volume of 6.3 km$^3$. The larger volume response is observed in the ELA perturbation experiment (Fig. 6d), where a non-linear variation appears between volume and the elevation of the ELA. Moving the ELA from the reference value (186 m a.s.l.) to 390 m a.s.l., the glacier loses 2.3 km$^3$, reaching 4.5 km$^3$ in ice volume. On the other hand, if the ELA decreases below sea level (which means that there is no ablation zone at the glacier surface; note that the frontal ablation is still considered in our model through the ice-ocean interface), the glacier gains about 1 km$^3$, reaching 7.8 km$^3$ in ice volume.

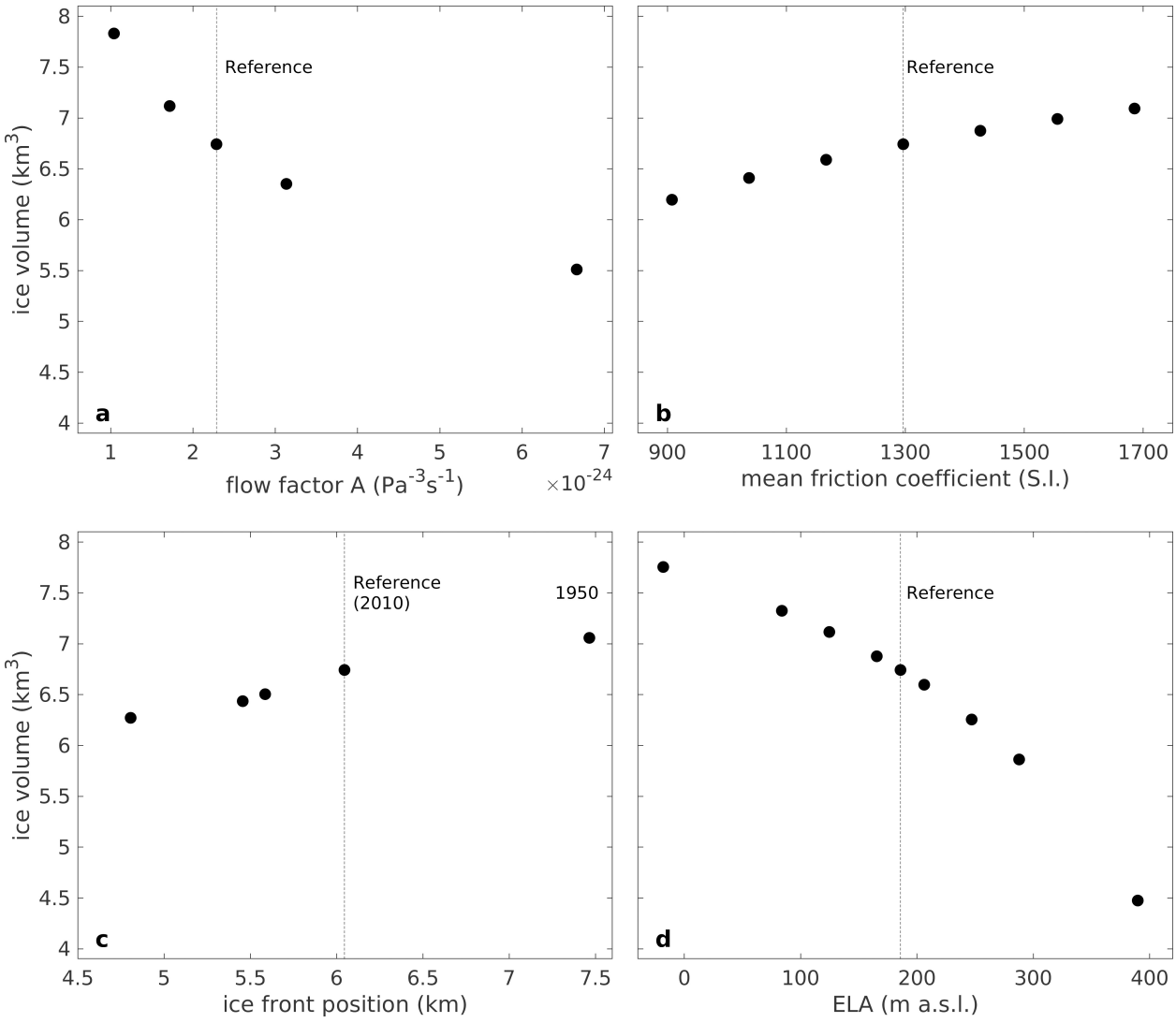


**Figure 6. Volume response to different perturbations: (a) flow rate factor, (b) friction coefficient, (c) ice front position, and (d) ELA. All experiments start from the same initial state.**

Figure 7 shows the resulting modeled steady state profile considering the 1950 ice front used in the centennial projections. Note that the 1950 ice cliff is close to a pronounced ridge in bed topography, located 100 m below sea level, from which the bedrock deepens sharply into the Admiralty Bay. This pronounced ridge may be a morainal bank (Cárdenas et al. 2020), suggesting a nearly stationary condition of the glacier, which reinforces the assumption made here (see the centennial response projections section). The initial state (2010) used in the centennial response analysis is shown in gray in Fig. 7. The figure also shows some of the front positions since 1950 as well as the reconstructed glacier profiles from 1950 to 2010. Note that the initial state is similar to the 2010 observed profile (black line in Fig. 7), and has an ice volume equal to 6.8 km$^3$. Considering the glacier state in 1950, the ice discharge is 0.0325 Gt/yr, whereas for the 2010 state, after imposing a retreat of the ice front, the discharge is 0.0342 Gt/yr. This represents an increase of ∼5% of glacier discharge over

the 1950-2010 period. Retreating the calving front position reduces the resistance provided by basal and lateral friction in the region of the terminus, increasing the ice velocity and the glacier discharge, consequently. Close to the 2010 glacier terminus, the velocity increases over than 30% in comparison to the 1950 velocities (Fig. 8a). The changes propagate inland mainly in regions controlled by basal drag (see Fig. 5c and Fig. 8a). In a hypothetical scenario where the entire amount of observed front retreat is imposed on the 1950 state, the instantaneous impact on the glacier velocity (e.g., Gudmundsson et al. 2019) produces a similar pattern of velocity changes, with the highest amount of speed-ups occurring mainly immediately upstream of the 2010 glacier terminus (Fig. 8b). The resultant glacier discharge is 0.0633 Gt/yr, i.e., an increase of 2× in ice flux compared to the 1950 state. These results show the control that the position of the glacier's terminus exerts on Lange's dynamics.

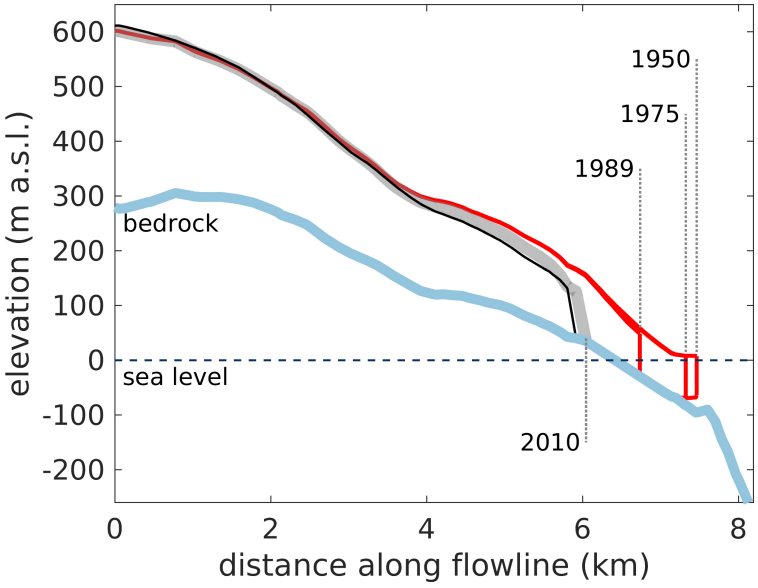


**Figure 7. Initial state setup for the centennial response analysis. The figure shows some of the front positions from 1950 to present day (2010), as well as the respective glacier profiles (red and gray lines). The ice profile for 1950 is obtained by assuming that the glacier was in steady state in 1950. From 1950 to 2010, we force the glacier to retreat following observed terminus positions. The 2010 profile (gray line) is the initial state used in the centennial response analysis. For comparison purposes, the figure also shows the 2010 observed surface elevation used in the model calibration phase (black line).**

The centennial glacier response to changes in ELA and calving position are shown in Fig. 9. Forcing Lange from 2010 to 2200 under the reference ELA (186 m a.s.l.) and under no changes in calving front yields a decrease of about 0.1 km$^3$ in ice volume in comparison to the initial state (2010), reaching ~6.7 km$^3$ (Fig. 9a). Most of the volume change happens by ~2050. Raising the ELA by 50 m produces ~0.4 km$^3$ of ice volume loss, almost 4× higher than with the reference ELA, reaching a volume equal to 6.4 km$^3$. If we increase the ELA to 330 m a.s.l., the resulting volume in 2200 is about 5.5 km$^3$, which is almost 20% less than the volume obtained with the reference ELA. Most of the volume loss occurs by ~2100, but the loss continues beyond 2200. Under a scenario where the ELA rises to 430 m a.s.l., the glacier's volume reduces to 4.0 km$^3$, a loss of 40% in comparison to the volume obtained with no changes in ELA. The glacier continues losing mass after 2200 at a relatively high rate (~0.042 km$^3$/decade). Note that, for this ELA scenario, the ice divide drops by ~70 m (Fig. 9c). Imposing a retreat of about 650 m in front position yields a volume loss of 0.2-0.3 km$^3$ higher than when the ice front is not changed, at least for ELA=186, 230, and 330 m a.s.l. (Fig. 9b). The ice volumes for these ELA scenarios are 6.4, 6.2, and 5.3 km$^3$, respectively. This additional mass loss is partly due to the imposed front retreat itself, i.e., the 'instantaneous' loss of volume at the beginning of the experiments (2010); the rest occurs dynamically over the years, as seen by the surface lowering observed mainly from kilometer 3 onwards, where the

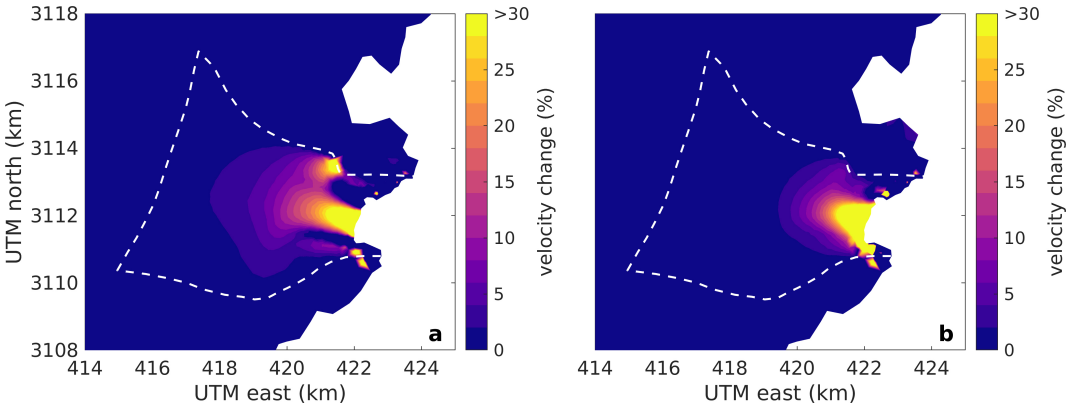


**Figure 8.** **Changes in surface velocity relative to the 1950 state: (a) 2010 state used as the initial state for the centennial response analysis; (b) instantaneous response to imposed observed ice front retreat. The 2010 state is obtained by a transient simulation starting in 1950 forced by observed retreat in calving front positions (see Table III). The instantaneous response is obtained by computing the ice velocity after imposing the entire amount of observed front retreat on the 1950 state. Only positive velocity changes (acceleration) are shown.**

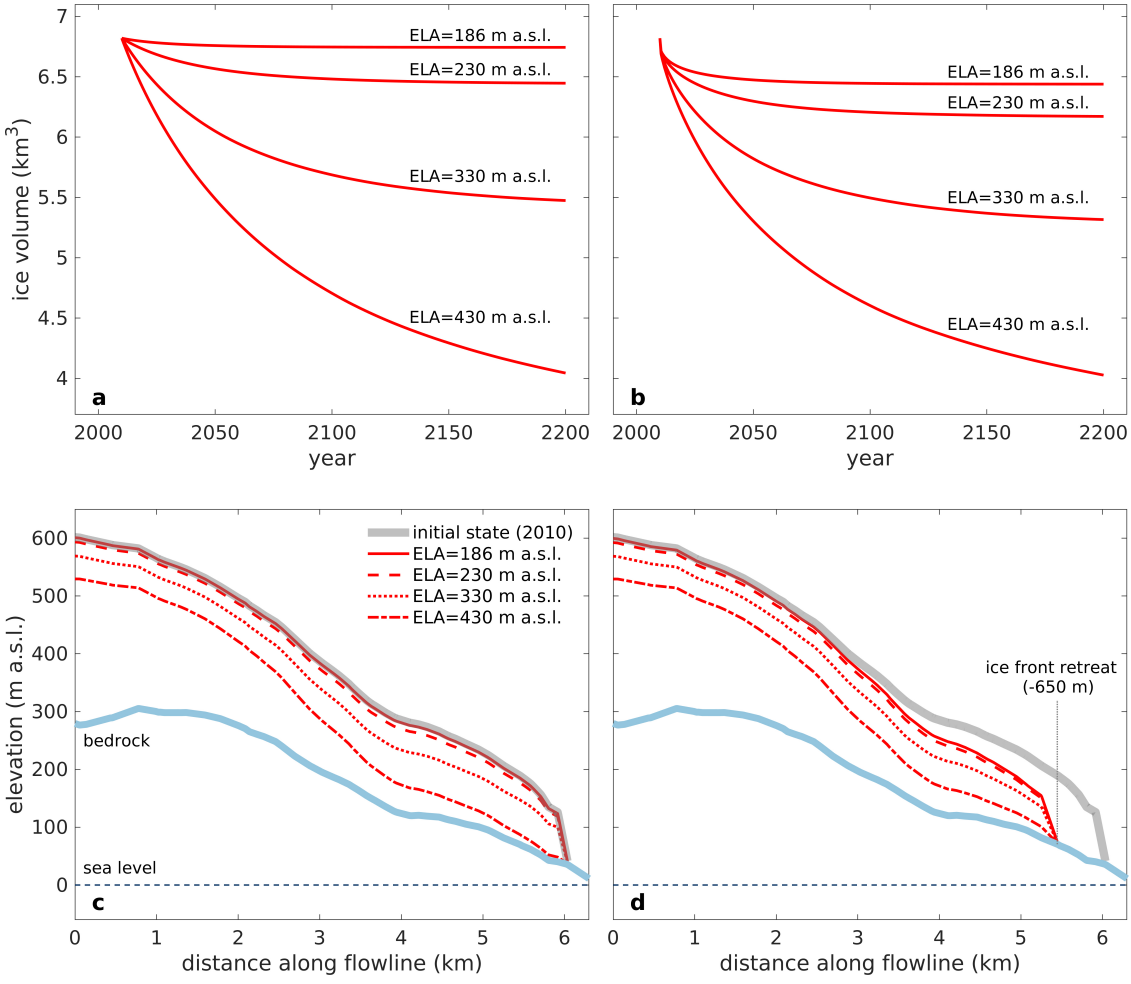


**Figure 9.** **Centennial response analysis: (a) and (b) show the ice volume evolution from the initial state (2010) to 2200 under different ELA scenarios, and (c) and (d) show the resulting glacier's profiles in 2200 (red lines). Solid-gray lines shown in (c) and (d) are the initial state profile (2010). In (b) and (c), a front retreat of 650 m is imposed at the beginning of the centennial response experiments (2010).**

flow is controlled by basal sliding (Fig. 9d). The time response of these adjustments in ice volume is similar to the case forced with the 2010 front position (Fig. 9a and b). Under a more drastic increase in ELA (i.e., ELA=430 m a.s.l.), the glacier reaches a similar volume as the one forced by no perturbation in front position, 4.0 $km^3$ (Fig. 9d), and the thickness reaches a 'minimum' value at Lange's terminus. The ice divide also drops by about 70 m compared to the initial state.

## DISCUSSION

In the dynamic calibration, only a non-spatially uniform distribution of the friction coefficient (Fig. 5b) leads to an acceptable agreement between modelled and observed surface elevations and surface velocities. Assuming a frozen bed (i.e., no basal slip), which is what previous studies relied on (e.g., Barboza et al. 2004), the model overestimates the ice surface especially in regions close to calving front, even with a relatively high flow rate factor, and underestimates the surface velocity in these areas (Fig. 4b). This strongly suggests that basal sliding plays an important role for most of Lange's domain, as seen by the extent of the regions of relatively low friction coefficient in Fig. 5b. The subglacial topography also suggests erosion rates that are consistent with basal sliding (Fig. 5a) as we find a narrow channel of relatively high flow velocity (300-500 m/yr, in Lange's case). This is consistent with the hypothesis of a temperate ice base (Blindow et al. 2010, Rückamp et al. 2010). Suspended sediments and freshwater discharge are frequently observed in front of Lange's terminus, suggesting that bedrock erosion is occurring (e.g., Pęcherzewski 1980, Pichlmaier et al. 2004, Aquino FE, unpublished data), which is in agreement with our modeling assumption that requires basal sliding to match observations. Note that, in this model calibration case (slip bed), we do not consider spatial variations in the flow rate factor *A*. Factors like heterogeneous distribution of temperature, water content, and the presence of surface crevasses impact the ice deformation. Taking all of these elements into a model calibration (i.e., tuning both the flow rate factor, *A*, and the friction coefficient, *C*) may improve the model dynamics. However, there is a risk of overturning such parameters in an unrealistic manner, besides the possible existence of multiple solutions for *A* and *C* (e.g., see Fig. 3 in Åkesson et al. 2017, which shows that multiple combinations of *A* and *C* minimize the surface velocity misfit). Alternatively, employing a thermal model would help to constrain the value of *A*, since some in-situ temperature profiles at the glacier divide are available (e.g., Simões et al. 2004b, Breuer et al. 2006, Blindow et al. 2010).

The perturbation experiments allow to estimate the glacier's sensitivity to future warming and uncertainties in external forcings as well as model input parameters. The range of perturbations in *A* considered in this study means 30% of variations around the reference ice rigidity *B*. Similar variations ($\pm$30%) in the friction coefficient, *C*, leads to smaller changes in ice volume (Fig. 6a and b). Note, however, that the basal friction is obtained by $C^2$ (Eq. 6). This represents a change of 50-70% in basal stress. We attribute these differences in sensitivity primarily to: (i) changes in flow rate factor, *A*, that affects the ice flow everywhere, i.e., in regions experiencing sliding and in regions where the flow is dominated by internal deformation; and (ii) the imposed changes in friction coefficient are not strong enough to induce basal sliding in areas close to ice summit and basin divide, which would lead to higher volume loss. The imposed changes in the ELA represent variations of up to 100% around the reference value. The amplitude of the volume response due to ELA perturbations is partly due to the

non-linear feedback between glacier height and mass balance, which increases the glacier sensitivity to changes in ELA. Without this feedback, the volume response would be considerably smaller (e.g., Åkesson et al. 2017). Note that the calving position is fixed in all perturbation experiments. It may not be realistic since it is expected that the glacier length would vary with the evolution of the ice thickness. However, keeping a fixed front position allows us to investigate the glacier volume sensitivity on the actual glacier area without adding unnecessary complexity to our modeling exercise (i.e., calving dynamics).

In the centennial response analysis (from 2010 to 2200), we constrain the 2010 state by applying observed changes in calving front positions since the 1950s (Fig. 7). This approach is straightforward and avoids complex calibrations if calving dynamics was included in the model (e.g., Bondzio et al. 2018, Choi et al. 2018). We also keep the surface mass balance fixed in time from 1950 to 2010. However, it is likely that variations in ELA happened during this period (e.g., Sobota et al. 2015, Pudełko et al. 2018). Incorporating variations in ELA elevations would bring a more realistic state for 2010. Nevertheless, keeping a fixed ELA from 1950 to 2010 makes it possible to isolate the effect of the observed front retreat without imposing any other external perturbation, and allows us to estimate the impact of observed changes in calving positions on the glacier dynamics. In our model, the effects of the observed front retreat on the glacier's dynamics persist beyond 2010. As seen in Fig. 9a, forced by the reference ELA, the glacier takes 40-50 years to reach a new steady state after the retreat ceases. This suggests that Lange is still 'adjusting' to its change in terminus position. Considering that the climate forcing has also been changing since the 1950s, and that climate will continue to change in the future, it is very likely that Lange will continue to show volume changes over the coming decades. These results should be confirmed by future observations in surface elevation. Also, modeling calving dynamics may be essential to improve the forecasts of Lange's future, since the position of the ice front exerts such a control on the glacier discharge.

Our centennial response projections are based on simple variations in ELA. While this is a straightforward and useful approach for a glacier response study, reliable forecasts of Lange and KGI ice cap require more realistic accumulation rates, generally based on climate variability and different forcing scenarios (e.g., Ligtenberg et al. 2013). However, KGI and neighboring islands around the Peninsula Antarctica are smaller than the grid resolutions usually employed by global or regional climate models (Ligtenberg et al. 2013, van Wessem et al. 2016). Yet, alternative methods based on climate variables (e.g., temperature) may provide more reliable scenarios of mass balance (e.g., Davies et al. 2014). Also, marine terminating glaciers like Lange are also influenced by sea-bed topography and water depth, and the fluctuations in ice front (advance and/or retreat) may be independent of climate and surface processes (e.g., SMB). Additionally, at a centennial scale the glacier can change to a land-terminating glacier. Therefore, calving dynamics may be important for reliable forecasts of Lange, as already pointed out above.

## CONCLUSIONS

By employing a three-dimensional glacier model calibrated by satellite-based and in-situ datasets, we find that at least 50% of Lange's basin is temperate, i.e., basal velocity is non-negligible (>1 m/yr) over most of the glacier domain. In particular, 2 km upstream of the glacier terminus, we find a wide

distribution of low friction coefficient, mainly where the bed elevation remains below 200 m. a.s.l. In this region, the ice flow is primarily controlled by basal sliding, and therefore, ice-bed conditions play an important role on the glacier's dynamics. The perturbation experiments show that the glacier is more sensitive to changes in the flow rate factor than in the friction coefficient. This suggests that numerical thermal modeling and further measurements of ice temperature as well as water content would constrain the value of the flow rate parameter, improving the reliability of future modeling. The glacier is significantly more sensitive to perturbations in surface mass balance compared to the other parameters considered here. This suggests that the climate variability of this region plays an important role on the mass balance and, consequently, on the glacier's dynamics. Therefore, numerical simulations of the future of Lange and other glaciers on King George Island would benefit from reliable projections of surface mass balance on the island. Transient simulations forced by a 60-year record of terminus position show that the observed calving front retreat induced a speed-up of the main ice stream by reducing basal and lateral friction exerted on this fast-flow region. Our model estimates that the front retreat was responsible for an increase over than 30% in ice velocity mainly in the region close to the 2010 terminus and an increase of at least 5% in the glacier discharge since 1950. In our transient simulations, the effects of the observed front retreat persist beyond 2010. This suggests that Lange is still adjusting to past perturbations at its terminus. Hence, calving dynamics may also be essential to forecast Lange's future.

**Acknowledgments**

This work was performed at the University of Campinas (UNICAMP) and Federal University of Rio Grande do Sul (UFRGS) with financial support from the Brazilian National Institute for Cryospheric Sciences (INCT da Criosfera), CNPq N° 465680/2014-3, and from the Conselho Nacional de Desenvolvimento Científico e Tecnológico (CNPq), PhD scholarship N° 140186/2015-8 - and at the University of California Irvine (UCI) under a contract with the National Aeronautics and Space Administration (NASA), Cryospheric Sciences Program (N° NNX14AN03G). Philippe Devloo was supported by CNPq under grant N° 305823/2017-5. We thank Fabio Magrani for kindly sharing the Admiralty Bay bathymetry.

## REFERENCES

ÅKESSON H, NISANCIOGLU KH, GIESEN RH & MORLIGHEM M. 2017. Simulating the evolution of Hardangerjøkulen ice cap in southern Norway since the mid-Holocene and its sensitivity to climate change. Cryosphere 11(1): 281-302. doi:10.5194/tc-11-281-2017. URL https://tc.copernicus.org/articles/11/281/2017/.

BARBOZA HHC, BORTOLI AL, SIMÕES JC, CUNHA RD & BRAUN M. 2004. Bidimensional numerical simulation of the Lange Glacier, King George Island, Antarctica. Pesq Antart Bras 4: 67-76.

BARRAND NE, VAUGHAN DG, STEINER N, TEDESCO M, KUIPERS MUNNEKE P, VAN DEN BROEKE MR & HOSKING JS. 2013. Trends in Antarctic Peninsula surface melting conditions from observations and regional climate modeling. J Geophys Res Earth Surf 118(1): 315-330. doi:https://doi.org/10.1029/2012JF002559. URL https://agupubs.onlinelibrary.wiley.com/doi/abs/10.1029/2012JF002559.

BERS AV, MOMO F, SCHLOSS IR & ABELE D. 2013. Analysis of trends and sudden changes in long-term environmental data from King George Island (Antarctica): relationships between global climatic oscillations and local system response. Clim Change 116(3): 789-803. doi:10.1007/s10584-012-0523-4. URL https://doi.org/10.1007/s10584-012-0523-4.

BINTANJA R. 1995. The local surface energy balance of the Ecology Glacier, King George Island, Antarctica: measurements and modelling. Antarct Sci 7: 315-325.

BLATTER H. 1995. Velocity and stress-fields in grounded glaciers: A simple algorithm for including deviatoric stress gradients. J Glaciol 41(138): 333-344.

BLINDOW N, SUCKRO SK, RÜCKAMP M, BRAUN M, SCHINDLER M, BREUER B, SAURER H, SIMÕES JC & LANGE MA. 2010. Geometry and thermal regime of the King George Island ice cap, Antarctica, from GPR and GPS. Ann Glaciol 51(55): 103–109. doi:10.3189/172756410791392691.

BONDZIO JH, MORLIGHEM M, SEROUSSI H, WOOD MH & MOUGINOT J. 2018. Control of Ocean Temperature on Jakobshavn Isbræ's Present and Future Mass Loss. Geophys Res Lett 45(23): 12,912-12,921. doi:https://doi.org/10.1029/2018GL079827.

URL https://agupubs.onlinelibrary.wiley.com/doi/abs/10.1029/2018GL079827.

BONGRAIN M & GODFROY RE. 1912. Deuxième expédition antarctique française (1908-1910), commandée par le Dr Jean Charcot: sciences physiques: documents scientifiques. URL https://www.sudoc.fr/113362501. 1 vol. (XI f. de dépl.): cartes; 28 cm.

BRAUN M, SAURER H, VOGT S, SIMÕES JC & GOßMANN H. 2001. The influence of large-scale atmospheric circulation on the surface energy balance of the King George Island ice cap. Int J Climatol 21: 21-36.

BRAUN M, SAURER H & GOSSMANN H. 2004. Climate, energy fluxes and ablation rates on the ice cap of King George Island. Pesq Antart Bras 4: 87-103.

BRAUN MH, BETSCH T & SEEHAUS T. 2016. King George Island TanDEM-X DEM, link to GeoTIFF. doi:10.1594/PANGAEA.863567. URL https://doi.org/10.1594/PANGAEA.863567.

BREUER B, LANGE M & BLINDOW N. 2006. Sensitivity studies on model modifications to assess the dynamics of a temperate ice cap, such as that on King George Island, Antarctica. J Glaciol 52(177): 235-247. doi:10.3189/172756506781828683.

BUDD WF, KEAGE PL & BLUNDY NA. 1979. Empirical Studies of Ice Sliding. J Glaciol 23(89): 157-170. doi:10.1017/S0022143000029804.

CARRASCO J. 2013. Decadal Changes in the Near-Surface Air Temperature in the Western Side of the Antarctic Peninsula. Atmos Clim Sci 3: 275-281. doi:10.4236/acs.2013.33029.

CHOI Y, MORLIGHEM M, WOOD M & BONDZIO JH. 2018. Comparison of four calving laws to model Greenland outlet glaciers. Cryosphere 12(12): 3735-3746. doi:10.5194/tc-12-3735-2018. URL https://www.the-cryosphere.net/12/3735/2018/.

COMIN AN & JUSTINO F. 2017. Investigação Climatológica na Península Antártica e no Arquipélago das Shetland do Sul. Anu Inst Geociênc 40(2): 74-81. doi:http://dx.doi.org/10.11137/2017_2_74_81.

COOK AJ, FOX AJ, VAUGHAN DG & FERRIGNO JG. 2005. Retreating Glacier Fronts on the Antarctic Peninsula over the Past Half-Century. Science 308(5721): 541-544. doi:10.1126/science.1104235. URL https://science.sciencemag.org/content/308/5721/541.

CUFFEY K & PATERSON WSB. 2010. The Physics of Glaciers. 4th ed. Oxford: Elsevier. 704 p.

CÁRDENAS C, CASASSA G, AGUILAR X, MOJICA D, JOHNSON E & BRONDI F. 2020. From Space to Earth: physical and biological impacts of glacier dynamics in the marine system by means of Remote Sensing at Almirantazgo Bay, Antarctica. In: 2020 IEEE Latin American GRSS & ISPRS Remote Sensing Conference (LAGIRS). p. 308-312. doi:10.1109/LAGIRS48042.2020.9165686.

DAVIES BJ, GOLLEDGE NR, GLASSER NF, CARRIVICK JL, LIGTENBERG SRM, BARRAND NE, VAN DEN BROEKE MR, HAMBREY MJ & SMELLIE JL. 2014. Modelled glacier response to centennial temperature and precipitation trends on the Antarctic Peninsula. Nat Clim Change 4: 993-998. doi:10.1038/nclimate2369.

DUVAL P. 1977. The role of the water content on the creep rate of polycrystalline ice. International Association of Hydrological Sciences Publication 118 (*Symposium at Grenoble 1975* - Isotopes and Impurities in Snow and Ice) p. 29-33.

FALK U, GIESEKE H, KOTZUR F & BRAUN M. 2016. Monitoring snow and ice surfaces on King George Island, Antarctic Peninsula, with high-resolution TerraSAR-X time series. Antarct Sci 28(2): 135-149. doi:10.1017/S0954102015000577.

FALK U, LÓPEZ DA & SILVA-BUSSO A. 2018a. Multi-year analysis of distributed glacier mass balance modelling and equilibrium line altitude on King George Island, Antarctic Peninsula. Cryosphere 12: 1211-1232. doi:10.5194/tc-12-1211-2018.

FALK U, SILVA-BUSSO A & PÖLCHER P. 2018b. A simplified method to estimate the run-off in Periglacial Creeks: a case study of King George Islands, Antarctic Peninsula. Philos Trans A Math Phys Eng Sci 376(2122): 20170166. doi:10.1098/rsta.2017.0166. URL https://royalsocietypublishing.org/doi/abs/10.1098/rsta.2017.0166.

FERRIGNO JG, COOK AJ, FOLEY KM, WILLIAMS JR RS, SWITHINBANK C, FOX AJ, THOMSON JW & SIEVERS J. 2006. Coastal-change and glaciological map of the Trinity Peninsula area and south Shetland Islands, Antarctica: 1843-2001: Chapter A in Coastal-change and glaciological maps of Antarctica. Tech rep. Survey, U.S. Geological. Reston, VA. doi:10.3133/i2600A. URL http://pubs.er.usgs.gov/publication/i2600A. Report.

FERRON FA, OES JCS, AQUINO FE & SETZER A. 2004. Air temperature time series for King George Island, Antarctica. Pesq Antart Bras 4: 155-169.

GONZALEZ S & FORTUNY D. 2018. How robust are the temperature trends on the Antarctic Peninsula? Antarct Sci 30(5): 322–328. doi:10.1017/S0954102018000251.

GUDMUNDSSON GH, PAOLO FS, ADUSUMILLI S & FRICKER HA. 2019. Instantaneous Antarctic ice sheet mass loss driven by thinning ice shelves. Geophys Res Lett 46(23): 13903-13909. doi:10.1029/2019GL085027. URL https://agupubs.onlinelibrary.wiley.com/doi/abs/10.1029/2019GL085027.

HAN J, XIE Z, DAI F & ZHANG W. 1999. Volcanic eruption recorded in an ice core from Collins ice cap, King George Island, Antarctica. Ann Glaciol 29: 121-125.

JIAWEN R, DAHE Q, PETIT JR, JOUZEL J, WENTI W, CHEN L, XIAOJUN W, SONGLIN Q & XIAOXIANG W. 1995. Glaciological studies on Nelson Island, South Shetland Islands, Antarctica. J Glaciol 41(138): 408-412. doi:10.3189/S0022143000016270.

JÓHANNESSON T, RAYMOND C & WADDINGTON E. 1989. Time-Scale for Adjustment of Glaciers to Changes in Mass Balance. J Glaciol 35(121): 355–369. doi:10.3189/S002214300000928X.

JOHNSON E, FLORICIOIU D, SCHWALBE E, KOSCHITZKI R, MAAS HG, CARDENAS C & CASASSA G. 2020. CALVING DYNAMICS DERIVED FROM SATELLITE SAR DATA IN SUPPORT OF MASS BALANCE ESTIMATIONS IN LANGE GLACIER, ANTARCTICA. ISPRS Annals of the Photogrammetry, Remote Sensing and Spatial Information Sciences IV-3/W2-2020: 125-127. doi:10.5194/isprs-annals-IV-3-W2-2020-125-2020. URL https://isprs-annals.copernicus.org/articles/IV-3-W2-2020/125/2020/.

KEJNA M, LÁSKA K & CAPUTA Z. 1998. Recession of the Ecology Glacier (King George Island) in the period 1961-1996. In: Glowacki P & Bednarek J (Eds), Polish Polar Studies: 25th International Polar Symposium. p. 121-128. Warszawa: Institute of Geophysics of the Polish Academy of Sciences.

KEJNA M, ARAŹNY A & SOBOTA I. 2013. Climatic change on King George Island in the years 1948–2011. Pol Polar Res 34(2): 213-235. doi:10.2478/popore-2013-0004.

KNAP WH, OERLEMANS J & CABÉE M. 1996. Climate sensitivity of the ice cap of King George Island, South Shetland Islands, Antarctica. Ann Glaciol 23: 154-159. doi:10.3189/S0260305500013380.

LAROUR E, SEROUSSI H, MORLIGHEM M & RIGNOT E. 2012. Continental scale, high order, high spatial resolution, ice sheet modeling using the Ice Sheet System Model (ISSM). J Geophys Res Earth Surf 117(F1): 1-20. doi:10.1029/2011JF002140. URL https://agupubs.onlinelibrary.wiley.com/doi/abs/10.1029/2011JF002140.

LEE J, JIN YK, HONG JK, YOO HJ & SHON H. 2008. Simulation of a tidewater glacier evolution in Marian Cove, King George Island, Antarctica. Geosci J 12(1): 33-39. doi:10.1007/s12303-008-0005-x. URL https://doi.org/10.1007/s12303-008-0005-x.

LIGTENBERG SRM, VAN DE BERG WJ, VAN DEN BROEKE MR, RAE JGL & VAN MEIJGAARD E. 2013. Future surface mass balance of the Antarctic ice sheet and its influence on sea level change, simulated by a regional atmospheric climate model. Clim Dyn 41(3): 867-884. doi:10.1007/s00382-013-1749-1. URL https://doi.org/10.1007/s00382-013-1749-1.

MACHERET Y & MOSKALEVSKY M. 1999. Study of Lange Glacier on King George Island, Antarctica. Ann Glaciol 29: 202–206. doi:10.3189/172756499781820941.

MAGRANI FJ & NETO A. 2014. Seismic characteristics and sedimentary distribution on the South Shetland Islands continental margin, Antarctica. Rev Bras Geof 32(3): 549-560. doi:10.22564/rbgf.v32i3.509. URL https://sbgf.org.br/revista/index.php/rbgf/article/view/509.

MARTÍN C, NAVARRO F, OTERO J, CUADRADO ML & CORCUERA MI. 2004. Three-dimensional modelling of the dynamics of Johnsons Glacier, Livingston Island, Antarctica. Ann Glaciol 39: 1–8. doi:10.3189/172756404781814537.

OLIVA M, NAVARRO F, HRBÁČEK F, HERNÁNDEZ A, NÝVLT D, PEREIRA P, RUIZ-FERNÁNDEZ J & TRIGO R. 2017. Recent regional climate cooling on the Antarctic Peninsula and associated impacts on the cryosphere. Sci Total Environ 580: 210-223. doi:https://doi.org/10.1016/j.scitotenv.2016.12.030. URL https://www.sciencedirect.com/science/article/pii/S0048969716327152.

ORHEIM O & GOVORUKHA LS. 1982. Present-day glaciation in the South Shetland Islands. Ann Glaciol 3: 233-238.

OSMANOĞLU B, BRAUN M, HOCK R & NAVARRO F. 2013. Surface velocity and ice discharge of the ice cap on King George Island, Antarctica. Ann Glaciol 54(63): 111–119. doi:10.3189/2013AoG63A517.

OTERO J, NAVARRO FJ, MARTÍN C, CUADRADO ML & CORCUERA MI. 2010. A three-dimensional calving model: numerical experiments on Johnsons Glacier, Livingston Island, Antarctica. J Glaciol 56(196): 200-214. doi:10.3189/002214310791968539.

PARK BK, CHANG SK, YOON HI & CHUNG H. 1998. Recent retreat of ice cliffs, King George Island, South Shetland Islands, Antarctic Peninsula. Ann Glaciol 27: 633–635. doi:10.3189/1998AoG27-1-633-635.

PASIK M ET AL. 2021. Glacier Geometry Changes in the Western Shore of Admiralty Bay, King George Island over the Last Decades. Sensors 21(4). doi:10.3390/s21041532. URL https://www.mdpi.com/1424-8220/21/4/1532.

PATTYN F. 2003. A new three-dimensional higher-order thermomechanical ice sheet model: Basic sensitivity, ice stream development, and ice flow across subglacial lakes. J Geophys Res Solid Earth 108(B8). doi:https://doi.org/10.1029/2002JB002329. URL https://agupubs.onlinelibrary.wiley.com/doi/abs/10.1029/2002JB002329.

PICHLMAIER M, AQUINO F, DA-SILVA C & BRAUN M. 2004. Suspended sediments in Admiralty Bay, King George Island (Antarctica). Pesq Antart Bras 4: 77-85.

PĘCHERZEWSKI K. 1980. Distribution and quantity of suspended matter in Admiralty Bay (King George Island, South Shetland Islands). Pol Polar Res 1: 75-82.

POLLARD D & DECONTO RM. 2012. A simple inverse method for the distribution of basal sliding coefficients under ice sheets, applied to Antarctica. Cryosphere 6(5): 953-971. doi:10.5194/tc-6-953-2012. URL https://tc.copernicus.org/articles/6/953/2012/.

PUDEŁKO R, ANGIEL PJ, POTOCKI M, JĘDREJEK A & KOZAK M. 2018. Fluctuation of Glacial Retreat Rates in the Eastern Part of Warszawa Icefield, King George Island, Antarctica, 1979–2018.

Remote Sens 10(6). doi:10.3390/rs10060892. URL https://www.mdpi.com/2072-4292/10/6/892.

ROSA KKD, PERONDI C, VEETTIL BK, AUGER JD & SIMÕES JC. 2020. Contrasting responses of land-terminating glaciers to recent climate variations in King George Island, Antarctica. Antarct Sci 32(5): 398–407. doi:10.1017/S0954102020000279.

RÜCKAMP M & BLINDOW N. 2012. King George Island ice cap geometry updated with airborne GPR measurements. Earth Syst Sci Data 4(1): 23-30. doi:10.5194/essd-4-23-2012. URL https://essd.copernicus.org/articles/4/23/2012/.

RÜCKAMP M, BLINDOW N, SUCKRO SK, BRAUN M & HUMBERT A. 2010. Dynamics of the ice cap on King George Island, Antarctica: field measurements and numerical simulations. Ann Glaciol 51(55): 80-90.

RÜCKAMP M, BRAUN M, SUCKRO S & BLINDOW N. 2011. Observed glacial changes on the King George Island ice cap, Antarctica, in the last decade. Glob Planet Change 79: 99-109.

SCAR-ADD. 2021. Antarctic Digital Database, online map viewer. URL https://www.add.scar.org/. Last access: 16 March 2021.

SCHWALBE E, KOSCHITZKI R, JOHNSON E, MONCADA DFM, SCHRÖTER B, CARDENAS C, CASASSA G & MAAS HG. 2020. Stereo-Photogrammetric Measurement Of Spatio-Temporal Velocity Fields At Lange Glacier, King George Island. In: 2020 IEEE Latin American GRSS & ISPRS Remote Sensing Conference (LAGIRS). p. 270-272. doi:10.1109/LAGIRS48042.2020.9165565.

SILVA AB, ARIGONY-NETO J, BRAUN MH, ESPINOZA JMA, COSTI J & NA RJ. 2020. Spatial and temporal analysis of changes in the glaciers of the Antarctic Peninsula. Glob Planet Change 184: 103079. doi:https://doi.org/10.1016/j.gloplacha.2019.103079. URL https://www.sciencedirect.com/science/article/pii/S0921818119305648.

SIMÕES CL, ROSA KKD, CZAPELA FF, VIEIRA R & SIMÕES JC. 2015. Collins Glacier Retreat Process and Regional Climatic Variations, King George Island, Antarctica. Geogr Rev 105(4): 462-471. doi:10.1111/j.1931-0846.2015.12091.x. URL https://doi.org/10.1111/j.1931-0846.2015.12091.x.

SIMÕES JC, BREMER UF, AQUINO FE & FERRON FA. 1999. Morphology and variations of glacial drainage basins in the King George Island ice field, Antarctica. Ann Glaciol 29: 220–224. doi:10.3189/172756499781821085.

SIMÕES JC, DANI N, BREMER UF, AQUINO FE & ARIGONY-NETO J. 2004a. Small cirque glaciers retreat on Keller Peninsula, Admiralty Bay, King George Island, Antarctica. Pesq Antart Bras 4: 49-56.

SIMÕES JC, FERRON FA, ARISTARAIN AJ, BERNARDO RT, STIEVENARD M & POURCHET M. 2004b. Ice core study from the King George Island ice cap, South Shetlands, Antarctica. Pesq Antart Bras 4: 9-23.

SOBOTA I, KEJNA M & ARAŹNY A. 2015. Short-term mass changes and retreat of the Ecology and Sphinx glacier system, King George Island, Antarctic Peninsula. Antarct Sci 27(5): 500–510. doi:10.1017/S0954102015000188.

SZIŁO J & BIALIK RJ. 2018. Recession and Ice Surface Elevation Changes of Baranowski Glacier and Its Impact on Proglacial Relief (King George Island, West Antarctica). Geosciences 8(10). doi:10.3390/geosciences8100355. URL https://www.mdpi.com/2076-3263/8/10/355.

THOMAS ER & TETZNER DR. 2019. The Climate of the Antarctic Peninsula during the Twentieth Century: Evidence from Ice Cores. In: Kanao M, Toyokuni G & yuki Yamamoto M (Eds), Antarctica. chap. 6. Rijeka: IntechOpen. doi:10.5772/intechopen.81507. URL https://doi.org/10.5772/intechopen.81507.

TRAVASSOS JM, PUERTAS LAP & SIMÕES JC. 2012. GPR signatures of temperate and cold land ice. Pesq Antart Bras 5: 137-151.

TURNER J, COLWELL SR, MARSHALL GJ, LACHLAN-COPE TA, CARLETON AM, JONES PD, LAGUN V, REID PA & IAGOVKINA S. 2005. Antarctic climate change during the last 50 years. Int J Climatol 25(3): 279-294. doi:10.1002/joc.1130. URL https://rmets.onlinelibrary.wiley.com/doi/abs/10.1002/joc.1130.

TURNER J, LU H, WHITE I, KING JC, PHILLIPS T, HOSKING JS, BRACEGIRDLE TJ, MARSHALL GJ, MULVANEY R & DEB P. 2016. Absence of 21st century warming on Antarctic Peninsula consistent with natural variability. Nature 535(7612): 411-415. doi:10.1038/nature18645. URL https://doi.org/10.1038/nature18645.

VAN WESSEM JM ET AL. 2016. The modelled surface mass balance of the Antarctic Peninsula at 5.5 km horizontal resolution. Cryosphere 10(1): 271-285. doi:10.5194/tc-10-271-2016. URL https://tc.copernicus.org/articles/10/271/2016/.

WEN J, KANG J, HAN J, XIE Z, LIU L & WANG D. 1998. Glaciological studies on King George Island ice cap, South Shetland Islands, Antarctica. Ann Glaciol 27: 105-109.

ZAMORUYEV VV. 1972. Results of glaciological observations at Bellingshausen station in 1968. Trudy Sov Antark Eksped 55: 135-144.

**How to cite**

SANTOS TD, MORLIGHEM M, SIMÕES JC & DEVLOO PRB. 2023. Sensitivity analysis of a King George Island outlet glacier, South Shetlands, Antarctica. An Acad Bras Cienc 95: e20210560. DOI 10.1590/0001-3765202320210560.

*Manuscript received on April 20, 2021;*
*accepted for publication on May 10, 2022*

**THIAGO DIAS DOS SANTOS**[1,2,4]
https://orcid.org/0000-0001-8257-1314

**MATHIEU MORLIGHEM**[3,4]
https://orcid.org/0000-0001-5219-1310

**JEFFERSON CARDIA SIMÕES**[2]
https://orcid.org/0000-0001-5555-3401

**PHILIPPE REMY BERNARD DEVLOO**[5]
https://orcid.org/0000-0002-8225-1107

[1]Universidade de São Paulo, Departamento de Engenharia Mecânica, Escola Politécnica, Av. Prof. Mello Moraes 2231, 05508-030 São Paulo, SP, Brazil
[2]Universidade Federal do Rio Grande do Sul, Centro Polar e Climático, Instituto de Geociências, Av. Bento Gonçalves 9500, 91501-970 Porto Alegre, RS, Brazil
[3]Dartmouth College, Department of Earth Sciences, Fairchild Hall, 19 Fayerweather Hill Road, 03755-3716, Hanover, NH, USA
[4]University of California, Department of Earth System Science, School of Physical Sciences, Irvine, 3200 Croul Hall, Irvine, 92697-3100, Irvine, CA, USA
[5]Universidade Estadual de Campinas, Departamento de Estruturas, Faculdade de Engenharia Civil, Arquitetura e Urbanismo, R. Saturnino de Brito 224, 13083-889 Campinas, SP, Brazil

Correspondence to: **Thiago Dias dos Santos**
*E-mail: santos.td@gmail.com*

## Author contributions

TDS designed the experimental setup and performed the numerical simulations. MM and PRBD guided the numerical glacier model. JCS guided the analyses of glaciological data. TDS led the analyses of the results and the initial writing of the paper. All authors contributed to writing the final version of the paper.